Single-atom Co-N$_3$ sites supported on waste paper-derived active carbon for synergistic adsorption and catalytic degradation of antibiotics

Mengying Qian [1], Meichi Lu [1], Minjia Yan, Chaofa Chen, Yuwen Hu, Yu Li, Jianrong Chen [*], Xi-Lin Wu [*]

College of Geography and Environmental Science, Zhejiang Normal University, Jinhua 321004, China

ARTICLE INFO

ABSTRACT

Single-atom catalysts (SACs) are emerging heterogeneous catalysts, which have been shown to be promising for a wide range of applications. Herein, we report the fabrication of single-atom Co sites with regulated Co-N$_3$ co-ordination supported on waste paper-derived active carbon (WPAC). The high specific surface area (535.2 m^2 g^{-1}) and active Co-N$_3$ single sites endowed the Co-N$_3$/WPAC with high adsorption capacity and excellent catalytic performance. The maximum adsorption capacity of sulfisoxazole (SIZ) onto Co-N$_3$/WPAC reached 274.5 mg g^{-1}, and the removal percentage of SIZ reached ~93.0 % within 1.0 min in the Co-N$_3$/WPAC+PS system. The bifunctional properties of Co-N$_3$/WPAC led to the efficient preconcentration of organic pollutants from aqueous solution as well as in-situ oxidation of them via the catalytic oxidation process. In addition, the Co-N$_3$/WPAC+PS system exhibited a wide operating pH range (3−11), high mineralization capacity (~89.3 %) and excellent reusability for the degradation of SIZ. Mechanism studies suggested that the Co-N$_3$ active sites were responsible for enhanced generation of the reactive oxygen species via PS activation, and both radical and non-radical processes contributed to the oxidation of SIZ. This work provides new insights into the resourceful disposal of waste paper and the application of SACs for environmental remediation.

1. Introduction

Antibiotics were once considered a medical miracle that had saved millions of lives [1]. However, abuse of antibiotics and inefficient sewage treatment processes have led to continuously discharging of them into the aquatic environment [2]. The long-term exposure to antibiotics has changed the environment of microbial habitat, resulting in the production of antibiotic resistance genes and antibiotics-resistant bacteria [3], finally posing potential risks to environment and human health [4,5]. Up to now, advanced oxidation processes (AOPs) have been explored extensively and identified to be state-of-the-art technologies for the treatment of recalcitrant organic wastewater [6,7]. In particular, persulfate-based AOPs (PS-AOPs) have gained ever-growing concerns due to the efficient production of reactive oxygen species (ROS) with high redox potential, including hydroxyl radicals ($\bullet$OH, E$_0$ = 2.8 V), sulfate radical (SO$_4^{\bullet-}$, E$_0$ = 2.5–3.1 V), superoxide radical (O$_2^{\bullet-}$, E$_0$ = 0.15 V) and singlet oxygen (^{1}O$_2$, E$_0$ = 2.2 V) [8,9]. In general, the ROS are generated via PS activation by using heat, ultrasonic, ultraviolet light,

transition metal (TM) ions, etc. [10]. Among these methods, transition metal catalysis is one of the most promising techniques for practical applications, owing to the higher efficiency, simpler operation and lower energy consumption. However, the homogeneous TM ions and heterogeneous TM nanoparticles usually suffer from high toxicity and low stability in acidic conditions. In recent years, increasing efforts have been made to develop robust and cost-effective TM catalysts for PS-AOPs.

Single-atom catalysts (SACs) with isolated nitrogen-coordinated metal atoms scattered on the carbon supports have attracted immense interest in heterogeneous catalysis by virtue of maximized atom utilization efficiency, tunable local electronic structures and excellent catalytic performance [11–13]. This is not only because the metal-nitrogen (M-N) coordination contributes to the formation of strong metal-support interactions, but also because the M-N moieties are proposed to be robust active centers for heterogeneous catalysis [14,15]. However, the cost-effective fabrication of SACs with abundant uniformly dispersed active sites on the surface of carbon matrix is still a challenge. Waste

---

paper is a low-cost, renewable and easily accessible material, mainly composed of cellulose [16]. Transformation of waste paper into energy or valuable products is a green and sustainable approach for waste paper disposal. Besides recycled paper manufacturing, researchers have embarked on efforts aimed to fabricate waste paper-derived materials for a wide range of applications. For instance, Tang et al. prepared activated carbon from waste paper as a porous adsorbent for removal of methylene blue from aqueous solution [17]. Yang et al. fabricated waste paper-derived magnetic nanocarbons and applied the nanocomposites to catalyze the synthesis of n-butyl levulinate from furfuryl alcohol [18]. Thus, waste paper as the easily available raw materials can be applied for fabrication of multifunctional carbon-based materials. In particular, the waste paper-derived nanocarbons can be used as the low-cost and robust support to anchor TM nanoparticles as well as the TM SACs.

Herein, single-atom Co sites with regulated Co-N$_3$ coordination supported on waste paper-derived active carbon (WPAC) were prepared. The low coordination number of the Co-N$_3$ sites could increase the charge density of the Co single atoms, leading to enhanced activity in the PS-AOPs [19]. The large surface area and abundant pore structure of Co-N$_3$/WPAC facilitated the exposure of single-atom metal sites for catalysis, as well as the transportation of reactants from aqueous solution to catalysts' surface. The Co-N$_3$/WPAC was applied for the removal of sulfisoxazole (SIZ), a model of the antibiotics, from water via PS activation. Effects of the initial solution pH, catalyst dosage, and PS concentration on SIZ degradation in the Co-N$_3$/WPAC+PS system were investigated. The generation of various ROS in the Co-N$_3$/WPAC+PS system was probed by using quenching experiments and electron paramagnetic resonance (EPR) measurements, and the underlying mechanisms were explored. This study will encourage researchers to synthesize valuable nanocatalysts from solid waste and provide a promising approach for practical wastewater treatment.

2. Materials and methods

2.1. Materials

Polyethyleneimine (PEI) was purchased from Alfa Aesar Chemical Co., Ltd. (Shanghai, China). 5,10,15,20-tetrakis(4-carboxyphenyl) porphyrin cobalt (TCPP-Co) was supplied by Jinan Henghua Science and Technology Co., Ltd. (Jinan, China). Hydrochloric acid (HCl), sodium hydroxide (NaOH), methanol (CH$_3$OH, MeOH), tert-butanol (C$_4$H$_{10}$O, TBA), ethanol (C$_2$H$_5$OH, EtOH), formic acid (HCOOH), phosphoric acid (H$_3$PO$_4$), acetonitrile (C$_2$H$_3$N, ACN), trifluoroacetic acid (CF$_3$COOH), triethylamine ((C$_2$H$_5$)$_3$N), sodium sulfate (Na$_2$SO$_4$) and potassium persulfate (K$_2$S$_2$O$_8$, PS) were provided by Sinopharm Chemical Reagent Co., Ltd. (Shanghai, China). Meropenem (C$_{17}$H$_{25}$N$_3$O$_5$S, MEM) was provided by Tianjin Guangfu Chemical Reagent Co., Ltd. (Tianjin, China). Norfloxacin (C$_{16}$H$_{18}$FN$_3$O$_3$, NOR), benzoquinone (C$_6$H$_4$O$_2$, BQ) and furfuryl alcohol (C$_5$H$_6$O$_2$, FFA) were obtained from Aladdin Chemical Co., Ltd. (Shanghai, China). Cefalexin (C$_{16}$H$_{19}$N$_3$O$_5$S, CL) was obtained from Shanghai Yuanye Bio-Technology Co., Ltd. (Shanghai, China). Sulfamethoxazole (C$_{10}$H$_{11}$N$_3$O$_3$S, SMX), sulfisoxazole (C$_{11}$H$_{13}$N$_3$O$_3$S, SIZ), 5,5-Dimethyl-1-pyrroline N-oxide (C$_6$H$_{11}$NO, DMPO) and 2,2,6,6-tetramethylpiperidine (C$_9$H$_{19}$N, TEMP) were purchased from Tokyo Chemical Industry Co., Ltd. (Tokyo, Japan). Tetracycline hydrochloride (C$_{22}$H$_{24}$N$_2$O$_8$·HCl, TCH) and chloroacetic acid (ClCH$_2$CO$_2$H) were supplied by Beijing J&K Scientific Co., Ltd. (Beijing, China). Nafion perfluorinated resin solution was purchased from Sigma-Aldrich Trading Co., Ltd. (Shanghai, China). The chemicals above were of analytical grade and used as received without further purification. Deionized water was prepared with Milli-Q ultra-pure water system (18.2 MΩ·cm).

2.2. Preparation of Co-N$_3$/WPAC

Waste paper (WP) was collected and pretreated by washing and

drying. The synthetic processes of Co-N$_3$/WPAC are illustrated in Scheme 1. First, 1.0 g of WP was weighed and added into a 250 mL conical flask with 100 mL of distilled water. After that, 2.5 g of NaOH and 2.5 g of ClCH$_2$COOH were added into the solution. The mixture was heated to 65 °C and held for 30 min, and then sonicated in water bath for 4 h. During the hydrothermal process, the -COOH groups were grafted onto the surface of WP. The obtained WP-COOH was washed, filtered and dried in a vacuum oven at 60 °C overnight. The negatively charged WP-COOH was then dispersed in 100 mL aqueous solution containing 0.08 g of PEI and 0.1 g of TCPP-Co. The mixture was continuously stirred for 12 h to achieve the full adsorption of PEI and TCPP-Co onto the WP-COOH. Then, the mixture was filtered, dried, and subsequently calcinated at 550 °C with a heating rate of 5 °C min^{-1} under N$_2$ atmosphere for 2 h, stepped by increasing the temperature to 700 °C with the same heating rate and kept for another 1 h. After cooling down to room temperature, the product was ground and treated by 1 M H$_2$SO$_4$ at 80 °C for 4 h, and finally washed with deionized water several times and dried at 60 °C under vacuum. For comparison, pure WPAC was prepared by calcination of the WP-COOH under the same procedure.

2.3. Characterizations and experimental procedure

The materials were characterized by using Scanning electron microscopy (SEM), transmission electron microscopy (TEM), aberration-corrected high-angle annular dark-field scanning TEM (HAADF-STEM), X-ray diffraction (XRD), X-ray absorption fine structure (XAFS), X-ray photoelectron spectroscopy (XPS), etc. Detailed characterizations of the samples are elaborated in **Text S1**.

Adsorption experiments were implemented in 10 mL sealed polyethylene tubes, containing desired concentration of SIZ and suspended Co-N$_3$/WPAC. The solution pH was adjusted to 6 by using 0.1 M NaOH or HCl. The samples were placed in a thermostatic water bath shaker with a shaking speed of 200 rpm at room temperature. Thereafter, 0.2 mL of the suspension was sampled at selected time intervals and filtered through a 0.22 μm membrane filter to separate Co-N$_3$/WPAC. The SIZ concentration in the separated solution was analyzed by high performance liquid chromatography (HPLC, Shimadzu 20AV). Details for the adsorption kinetics and adsorption isotherms are shown in **Text S2**.

Catalytic degradation of SIZ in the Co-N$_3$/WPAC+PS system was carried out in a 100 mL beaker at room temperature. The solution containing 20 mg L^{-1} of SIZ and 0.2 g L^{-1} of Co-N$_3$/WPAC was stirred for 30 min to establish the adsorption-desorption equilibrium. The solution pH was adjusted by 0.1 M HCl and NaOH. After that, PS was added into the solution under continuous stirring to trigger the catalytic oxidation process. At specific time intervals, 0.5 mL of the reaction solution was withdrawn and immediately filtered through a 0.22 μm membrane filter, and then quenched with excessive methanol. The catalyst was recycled by filtration after each run of the experiment and washed with deionized water thoroughly for the cycling experiment. Degradation of various antibiotics (NOR, SMX, TCH, MEM and CL) was carried out by using the same procedure. The concentrations of the antibiotics were determined by HPLC (details are summarized in Table S1). The removal of the total organic carbon (TOC) was performed in 400 mL of the solution containing 20 mg L^{-1} of SIZ and 0.2 g L^{-1} of Co-N$_3$/WPAC. After adding a certain amount of PS to trigger the oxidation process, 9 mL of the reaction solution was sampled at the required time intervals. The samples were filtered through a 0.22 μm membrane and immediately detected by a TOC analyzer.

3. Results and discussion

3.1. Structural and morphological characterizations

From the SEM images, one can observe that the surface of WPAC (Fig. S1a) was smooth, but Co-N$_3$/WPAC (Fig. S1b and Fig. 1a)
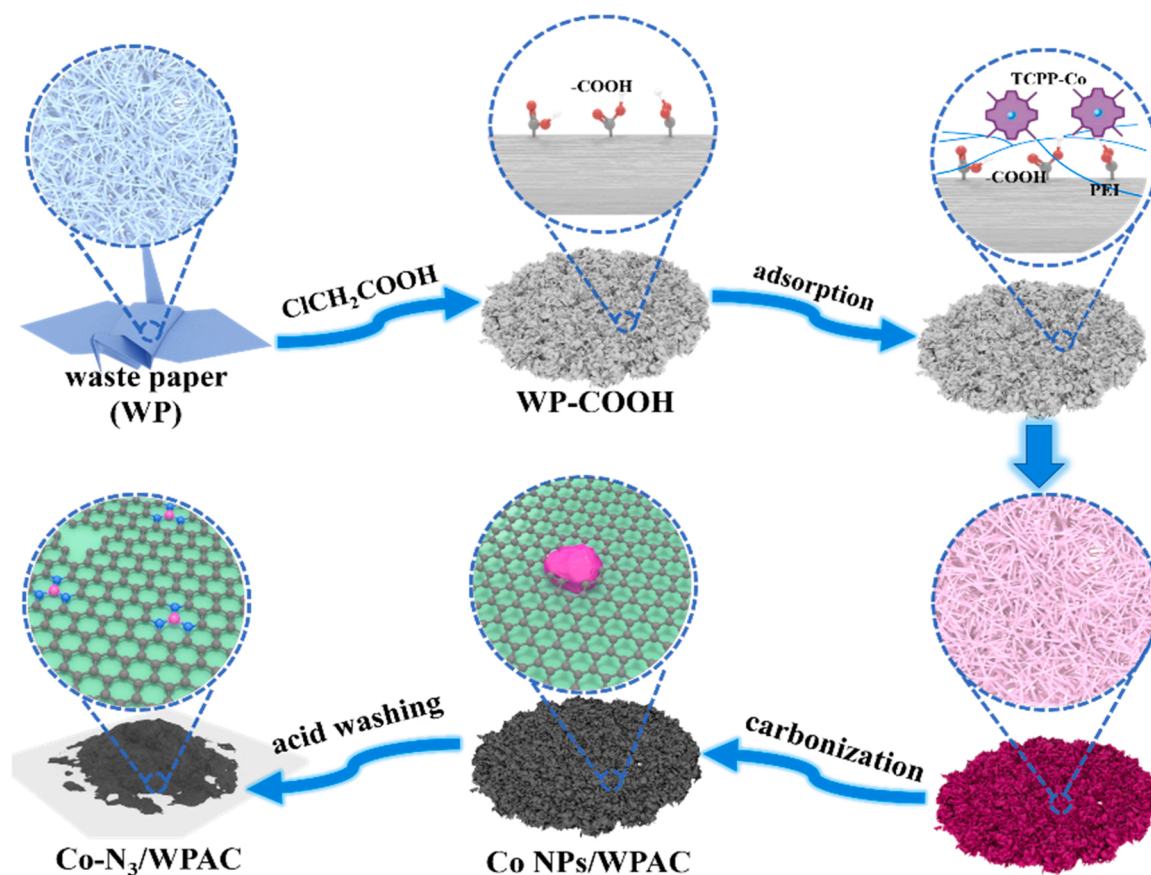
Scheme 1. Schematic illustration of the fabrication of Co-N$_3$/WPAC.

presented a rough surface with sea cucumber-like structure on its surface. TEM image of Co-N$_3$/WPAC (Fig. 1b) showed the presence of wrinkles and nanopores in the nanocarbons, which was beneficial to the exposure of more active surface sites for catalysis. None of the metal particles or clusters can be observed from the TEM image, indicating the Co species may be atomically anchored on the WPAC substrate. The HAADF-STEM image (Fig. 1c) of Co-N$_3$/WPAC clearly revealed that bright dots were densely distributed over the carbon matrix, corresponding to the atomically dispersed Co atoms. As shown in Fig. 1d, XRD patterns of WPAC and Co-N$_3$/WPAC exhibited two broad diffraction peaks, which were assigned to (002) and (100) planes of graphitic carbons [20]. As compared with pure WPAC, the (002) diffraction peak of Co-N$_3$/WPAC was shifted to a higher angle with deceased intensity, indicating poorer crystallinity and decreased interlayer spaces of the carbon skeleton [21,22]. Meanwhile, no peaks associated with metallic Co or Co oxides can be found in the XRD pattern of Co-N$_3$/WPAC, which also revealed the atomic dispersion of the Co species on the WPAC substrate.

Raman spectra of WPAC and Co-N$_3$/WPAC were shown in Fig. 1e, where the peaks located at 1300 and 1580 cm^{-1} were assigned to D and G bands, respectively [20]. The ratio of the peak intensities between D and G bands (I_D/I_G) reflected the degree of defect and disorder in the graphite carbons [20]. The calculated I_D/I_G value for Co-N$_3$/WPAC (0.79) was slightly larger than that for WPAC (0.74), implying the formation of more defects in the carbon lattices, which provided extra active sites for the heterogeneous catalysis. From the N$_2$ adsorption-desorption isotherm (Fig. 1f), the rapid and high N$_2$ adsorption at low relative pressures indicated the presence of abundant micropores in the Co-N$_3$/WPAC [23]. While the hysteresis loops arose at a relatively high pressure, attributing to the existence of mesopores in the Co-N$_3$/WPAC [20]. The pore size of Co-N$_3$/WPAC was mainly

located in the range of 0–10 nm (Fig. S2), confirming its mesoporous structure. The Brunauer–Emmett–Teller (BET) specific surface area of Co-N$_3$/WPAC was calculated to be 535.2 m^2 g^{-1}, much larger than that of WPAC (390.7 m^2 g^{-1}). The high specific surface area and abundant micro-/mesopores provided a large number of accessible active sites as well as the channels for mass transfer, thereby boosting the adsorption and the catalytic processes on the surface of Co-N$_3$/WPAC [20].

From the Co K-edge X-ray absorption near-edge structure (XANES) spectrum (Fig. 1g), the absorption edge of Co-N$_3$/WPAC was located between those of Co foil and CoO, suggesting that the valence state of Co single-atom sites in Co-N$_3$/WPAC was between 0 and + 2. The Fourier transforms k^3-weighted extended X-ray absorption fine structure (FT-EXAFS) curve of Co-N$_3$/WPAC (Fig. 1h) displayed a major peak at around 1.5 Å with the absence of the Co-Co peak, demonstrating the formation of Co-N coordination [24]. The wavelet transform (WT) EXAFS plot of Co-N$_3$/WPAC solely presented one intensity maximum at 4.1 Å (inset of Fig. 1i), confirming the formation of the Co-N$_x$ single-atom sites [25]. Furthermore, the EXAFS curve of Co-N$_3$/WPAC was fitted in both R (Fig. 1i) and k spaces (Fig. S3), and the corresponding fitting parameters were listed in Table S2. The best fitting results disclosed that the Co atoms were averagely coordinated by three N atoms with the average Co-N bond length of 1.9 Å, illustrating the Co-N$_3$ configuration in Co-N$_3$/WPAC. These results collectively demonstrated the successful fabrication of the single-atom Co-N$_3$ sites by using the low-cost WPAC as the support. The XPS survey of Co-N$_3$/WPAC unveiled the coexistence of C, N, O and Co elements (Fig. S4a). As shown in Fig. S4b, the high-resolution C 1 s spectra of WPAC and Co-N$_3$/WPAC were deconvoluted into three peaks, corresponding to the C-C, C-N/C=N and O-C=O chemical bonds, respectively [18,22]. The existence of C-N/C=N bonds in the Co-N$_3$/WPAC attested the successful introduction of N dopants into the carbon lattices,
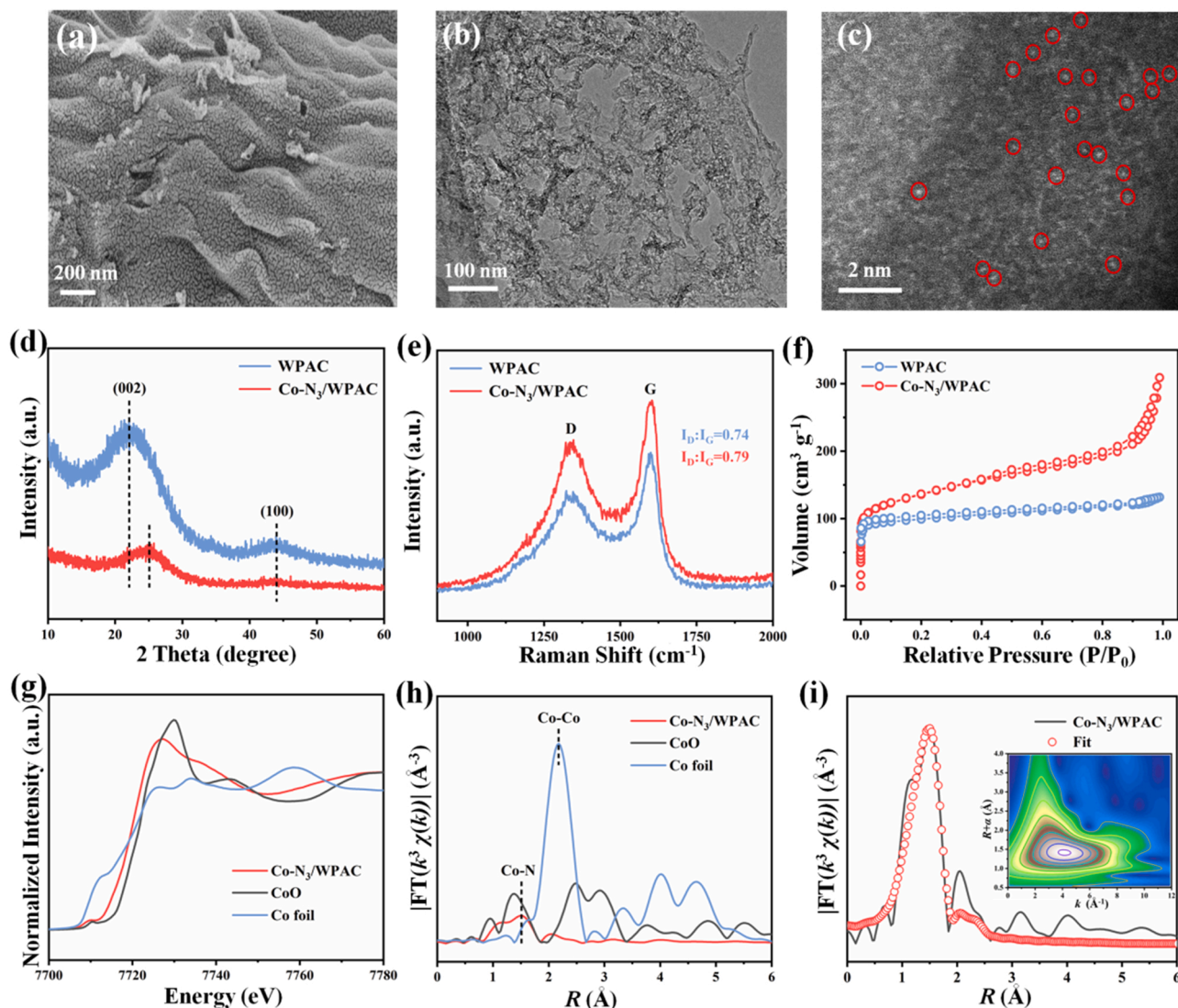
Fig. 1. (a) SEM, (b) TEM and (c) HAADF-STEM images of Co-N$_3$/WPAC. (d) XRD patterns and (e) Raman spectra of WPAC and Co-N$_3$/WPAC. (f) N$_2$ adsorption-desorption isotherms of Co-N$_3$/WPAC and WPAC. (g) Normalized Co K-edge XANES and (h) FT-EXAFS spectra of the Co-N$_3$/WPAC, CoO and Co foil. (i) EXAFS fitting curve of Co-N$_3$/WPAC at *R* space and wavelet transformed EXAFS spectrum.

providing abundant N sites for anchoring the Co single-atom sites. The N 1 s spectrum of Co-N$_3$/WPAC was deconvoluted into five peaks (Fig. S4c), which were identified as pyridinic N (398.4 eV), Co-N (399.1 eV), pyrrolic N (400.0 eV), graphitic N (401.2 eV), and oxidized N (405.1 eV), respectively [20]. The presence of the Co-N peak also validated the formation of Co-N coordination in the Co-N$_3$/WPAC. As compared with WPAC, the nitrogen contents in Co-N$_3$/WPAC, especially pyridinic N and graphitic N, were apparently increased, which provided additional active sites and facilitated the electron transfer for the catalytic process (Fig. S4c). Moreover, the peak of pyridinic N for Co-N$_3$/WPAC was shifted to lower binding energy as compared to that for WPAC, indicating that the Co single atoms were mainly bonded with pyridinic N atoms. Two major peaks centered at 781.3 eV (Co 2p$_{3/2}$) and 795.9 eV (Co 2p$_{1/2}$) in the Co 2p spectrum of Co-N$_3$/WPAC (Fig. S4d) confirmed the divalent state of the Co [26,27].

3.2. Adsorption performance of Co-N3/WPAC

The adsorption process described the transfer of molecules from the gas/liquid phase to the surface of the solid adsorbent. In order to better understand the adsorption process, the adsorption kinetics of SIZ onto Co-N$_3$/WPAC was studied. As shown in Fig. 2a, the adsorption of SIZ onto Co-N$_3$/WPAC increased sharply within the first 2 min, and then slowed down until reached the adsorption equilibrium within 20 min. Such super-fast adsorption kinetics suggested the presence of ample and available adsorption sites on the surface of Co-N$_3$/WPAC. The adsorption kinetics were fitted by the pseudo-first-order (Fig. 2b) and pseudo-second-order kinetic model (Fig. 2c), and the corresponding kinetic parameters and correlation coefficients were summarized in Table S3. The much higher correlation coefficient (R^2 = 0.9995) declared the perfect fitting of experimental data by the pseudo-second-order model.

The adsorption isotherm was plotted in Fig. 2d. The experiment result suggested that the equilibrium adsorption capacity (q_e) increased with the increase of SIZ equilibrium concentration, and reached the maximum at last. Langmuir and Freundlich models were employed to fit the adsorption isotherm and the corresponding fitting parameters were listed in Table S4. It was found that the Langmuir model better described the adsorption isotherm, indicating that the adsorption of SIZ onto Co-N$_3$/WPAC was monolayer and reversible [28]. The maximum adsorption capacity (q_{max}) of Co-N$_3$/WPAC toward SIZ was 274.5 mg g^{-1}, showing the superb adsorption performance of Co-N$_3$/WPAC, which might be due to its large specific surface area and porous structure. The
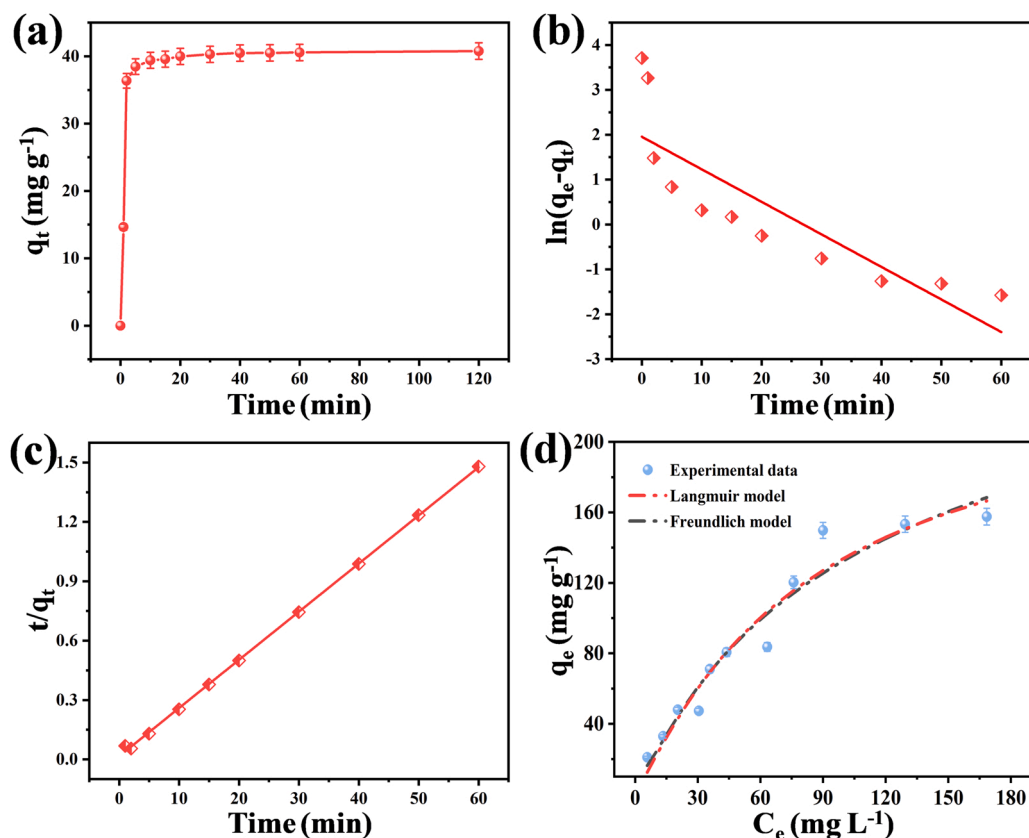
Fig. 2. (a) Adsorption kinetics of SIZ onto Co-N$_3$/WPAC, and the corresponding fitting plots of (b) pseudo-first-order model and (c) pseudo-second-order model. (d) Adsorption isotherm of SIZ onto Co-N$_3$/WPAC and the fitted curves (Experimental conditions: pH 6, [SIZ] = 10–200 mg L^{-1}, [Catalysts] = 0.2 g L^{-1}.).

excellent adsorption property could prompt the preconcentration of SIZ near the active centers of Co-N$_3$/WPAC, thus facilitating the catalytic degradation of SIZ by the in-situ generated ROS at the surface of Co-N$_3$/WPAC.

3.3. Catalytic performance of Co-N$_3$/WPAC for PS activation

The catalytic performance of Co-N$_3$/WPAC for PS activation was systematically investigated by using SIZ as a model of the antibiotics. Fig. 3a displayed the degradation of SIZ in the PS, WPAC+PS and Co-N$_3$/WPAC+PS systems under the same experimental conditions. The removal percentages of SIZ through adsorption by WPAC and Co-N$_3$/WPAC were 2.7 % and 33.4 %, respectively, confirming the enhanced adsorption performance of Co-N$_3$/WPAC. The catalytic oxidation process was triggered by adding PS into the reaction solution. The removal percentage of SIZ in the WPAC+PS system reached 20.2 % within 30 min, indicating the poor catalytic activity of WPAC toward PS activation. While the removal efficiency significantly increased to 93.0 % within 1 min and 99.6 % within 30 min in the Co-N$_3$/WPAC+PS system. Notably, PS alone was inefficient in the degradation of SIZ with only 3.5 % of SIZ was eliminated within 30 min. These results determined that the Co single sites contributed to the enhanced catalytic activity for PS activation. In addition, the doped N atoms in the WPAC may be also involved in the heterogeneous activation of PS [23]. The pseudo-first-order kinetic model was applied to fit the SIZ degradation kinetics in the various systems (**Text S3,** Fig. S5), and the corresponding kinetic rate constants (*k*) were listed in Table S5. As expected, the value of *k* (0.16 min^{-1}) for the Co-N$_3$/WPAC+PS system was about 16 times greater than that for the WPAC+PS system, confirming the enhanced performance of the Co-N$_3$/WPAC catalyst.

The effect of initial solution pH on SIZ removal in the Co-N$_3$/WPAC+PS system was explored (Fig. 3b). It was found that the

adsorption percentages of SIZ onto Co-N$_3$/WPAC were almost unchanged (35 %—38 %) over the tested pH range (pH 3–11). This suggested that the adsorption process was driven by the hydrophobic effect and π-π interactions between the benzene-ring of SIZ and sp^2 carbons of Co-N$_3$/WPAC [20]. The catalytic oxidation process was found to be efficient for SIZ degradation over a wide range of solution pH (3−11) with the SIZ degradation percentages all greater than 94 %. Meanwhile, Co ions leaching out from the Co-N$_3$/WPAC+PS system were monitored by inductively coupled plasma mass spectrometry (ICP-MS). As shown in Fig. S6, concentrations of Co ions in the Co-N$_3$/WPAC+PS system were all below 0.05 mg L^{-1} over the tested pH range (3−11), confirming high robustness and catalytic activity of the Co-N$_3$/WPAC catalyst. The PS and Co-N$_3$/WPAC dosages were optimized to be 0.5 g L^{-1} and 0.2 g L^{-1}, respectively (Fig. S7).

In comparison with the recently reported single-atomic site Cu (SAS-Cu) [29], MnFe$_2$O$_4$ supported on sludge-derived active carbon (MnFe$_2$O$_4$-SAC) [30], Co$_3$V$_2$O$_8$ [31], Bi$_2$O$_3$/CuNiFe layered double hydroxides (LDHs) [32], activated carbon coated with CoFe LDH (AC@CoFe-LDH) [33], Fe, N co-doped biochar (Fe-N-BC) [34], N-doped reduced graphene oxide (N-rGO) [35], γ-Fe$_2$O$_3$/CeO$_2$ [36], TiO$_2$ doped with acetylene black (TiO$_2$/AB) [37], N-doped biochar-loaded nanoscale zero-valent iron composites (Fe@N$_2$-BC$_{900}$) [38], Co$_3$O$_4$/CNTs [39], cellulose derived biochar (CBC-1000) [40] (Fig. 3c **and** Table S6), Co-N$_3$/WPAC presented superior catalytic performance in PS activation, with regard to the admirable normalized removal efficiency, fast elimination of contaminants, and low consumption of PS. Furthermore, the high TOC removal percentage (~89.3 %) implied excellent oxidation and mineralization capacities of Co-N$_3$/WPAC+PS system for the decomposition of SIZ into CO$_2$ and H$_2$O (Fig. 3d). The reusability and stability of the catalyst was vital for its practical application. As illustrated in Fig. S8, the removal percentages of SIZ were all larger than 95 % for the five consecutive cycles, indicating excellent stability and
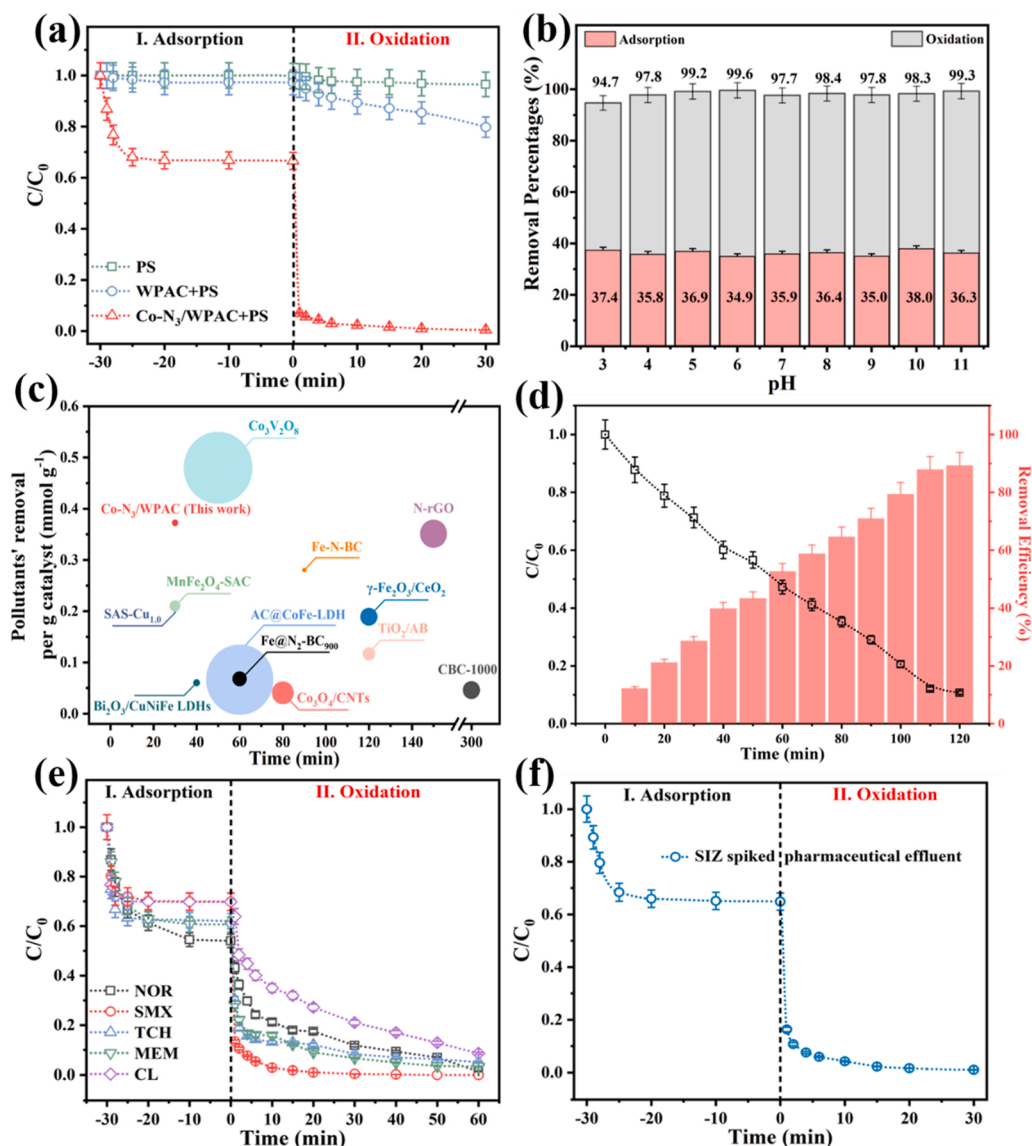
Fig. 3. (a) Degradation of PS in the PS, WPAC+PS and Co-N$_3$/WPAC+PS systems; (b) Effect of initial solution pH on SIZ removal in the Co-N$_3$/WPAC+PS system; (c) Comparison of Co-N$_3$/WPAC with the recently reported catalysts for degradation of organic pollutants via PS activation (diameter of the ball represents PS/pollutant ratio); (d) TOC removal in the Co-N$_3$/WPAC+PS system; (e) Degradation of various antibiotics and (f) SMX spiked pharmaceutical effluent in the Co-N$_3$/WPAC+PS system (Experimental conditions: pH 6, [SIZ] = 20 mg L^{-1}, [NOR] = [SMX] = [TCH] = [MEM] = [CL] = 10 mg L^{-1}, [Catalysts] = 0.2 g L^{-1}, [PS] = 0.5 g L^{-1}).

reusability of the Co-N$_3$/WPAC catalyst. The recycled Co-N$_3$/WPAC was characterized by XRD and XPS (Fig. S9, Fig. S4a), and no obvious changes in the structure and composition could be detected, confirming the outstanding stability of Co-N$_3$/WPAC. Besides SIZ (Fig. 3e), the various antibiotics (NOR, SMX, TCH, MEM and CL) can be effectively removed in the Co-N$_3$/WPAC+PS system via the combination of adsorption and catalytic oxidation processes. In addition, degradation of SIZ spiked pharmaceutical effluent in the Co-N$_3$/WPAC+PS system was also investigated (Fig. 3f). The result disclosed that SIZ removal percentage reached 99.0 % in the Co-N$_3$/WPAC+PS system, suggesting Co-N$_3$/WPAC mediated PS-AOPs was applicable for the removal of antibiotics from the real wastewater matrix. These results collectively demonstrated the great application potential of Co-N$_3$/WPAC catalyst for the treatment of antibiotic wastewater.

3.4. Identification of ROS and mechanism studies

Quenching experiments and EPR analysis were carried out to identify the generated ROS in the Co-N$_3$/WPAC+PS system. MeOH, TBA, BQ, and FFA were applied for scavenging $\bullet$OH/SO$_4^{\bullet-}$, $\bullet$OH, O$_2^{\bullet-}$, and ^{1}O$_2$, respectively [41,42]. As depicted in Fig. 4a and Fig. S10, the addition of MeOH or TBA significantly inhibited the degradation of SIZ with the

removal percentage falling to 59.3 % and 68.8 %, respectively. This verified the primary contribution of $\bullet$OH and SO$_4^{\bullet-}$ to the oxidation of SIZ. The degradation of SIZ was also suppressed by FFA, indicating that ^{1}O$_2$ may be involved in the catalytic oxidation process. However, it has been reported that high concentration of FFA may also react with $\bullet$OH and SO$_4^{\bullet-}$ [43]. Moreover, adding D$_2$O into the Co-N$_3$/WPAC+PS system to prolong the life-span of ^{1}O$_2$ presented no obvious impact on SIZ degradation (Fig. S11), implying that ^{1}O$_2$ played a minor role in the oxidation of SIZ. The presence of BQ can hardly affect SIZ degradation, suggesting that O$_2^{\bullet-}$ was irresponsible for the oxidation of SIZ. DMPO and TEMP were applied as the trapping agents for the EPR analysis in various systems. As compared with the WPAC+PS system (Fig. 4b), much stronger and prominent DMPO-$\bullet$OH and DMPO-SO$_4^{\bullet-}$ signals were detected in the Co-N$_3$/WPAC+PS system, indicating efficient generation of the radical species via Co-N$_3$/WPAC catalyzed PS activation. Similarly, as shown in Fig. 4c, the stronger triplet TEMP-^{1}O$_2$ signals were observed in the Co-N$_3$/WPAC+PS system than in the WPAC+PS system, suggesting the ^{1}O$_2$ as another ROS was produced via PS activation by using the Co-N$_3$/WPAC catalyst. No obvious DMPO-O$_2^{\bullet-}$ signals can be detected in the two systems (Fig. S12), ruling out the production of O$_2^{\bullet-}$ in the Fenton-like process. In comparison to the WPAC+PS system, the remarkably stronger EPR signals in the Co-N$_3$/WPAC+PS system
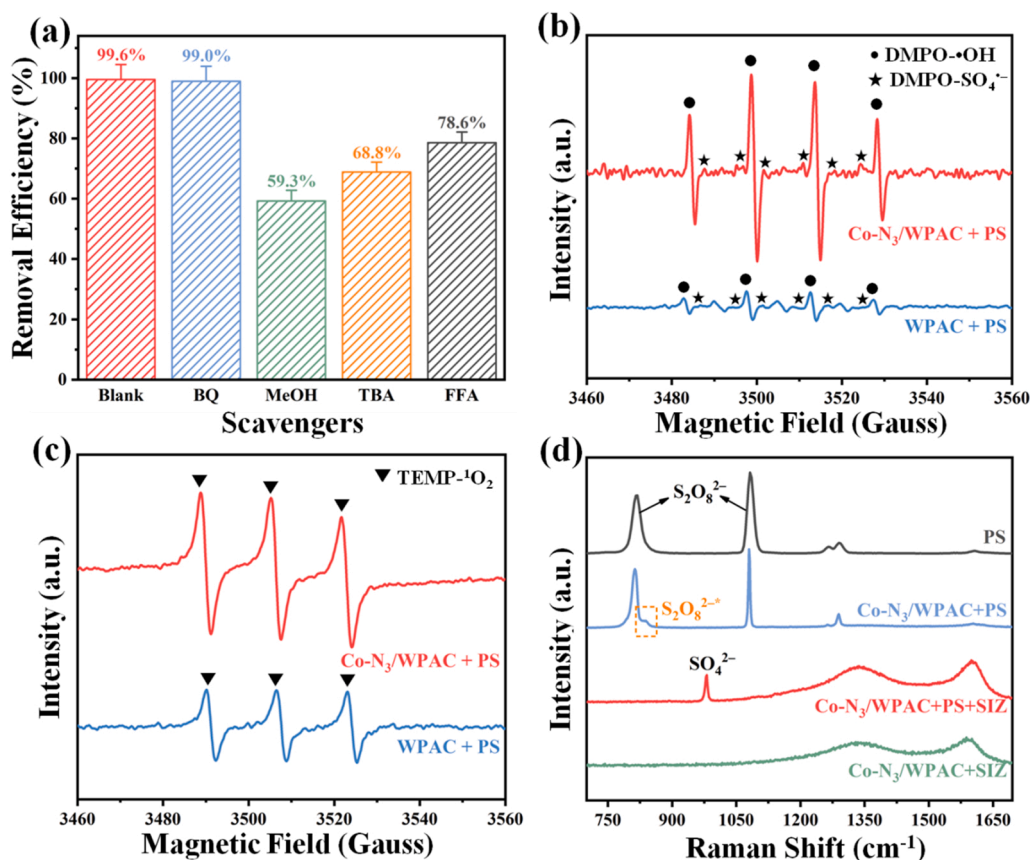
Fig. 4. (a) The removal efficiency of SIZ under various quenching conditions; EPR spectra of the Co-N$_3$/WPAC+PS system by using (b) DMPO and (c) TEMP as the trapping reagents ((●): DOMP-•OH adducts, (★): DMOPO-SO$_4^{•-}$ adducts, (▼): TEMP-^{1}O$_2$ adducts). (d) *In-situ* Raman spectra in different reaction systems (Experimental conditions: pH 6, [SIZ] = 20 mg L^{-1}, [Catalysts] = 0.2 g L^{-1}, [PS] = 0.5 g L^{-1}, [MeOH] = [TBA] = [BQ] = 100 mM, [FFA] = 0.8 g L^{-1}.).

corroborated that those Co-N$_3$ sites contributed to the enhanced catalytic performance of the Co-N$_3$/WPAC catalyst.

In-situ Raman spectroscopy was applied to probe the evolution of the PS molecules during the catalytic oxidation process. As shown in Fig. 4d, the bands centered at 815 and 1075 cm^{-1} were assigned to the S-O stretching vibration mode and the symmetric S═O stretching vibration mode of S$_2$O$_8^{2-}$, respectively [44]. Interestingly, a new peak (S$_2$O$_8^{2-*}$) at around 837 cm^{-1} emerged in the Co-N$_3$/WPAC+PS system, which could be due to the bending vibration of the elongated O-O bond in the metastable Co-N$_3$/WPAC-PS* intermediate [45–50], demonstrating the formation of the complex between PS and the Co-N$_3$/WPAC catalyst. The positively charged Co-N$_3$ sites as well as the graphitic N sites could be the adsorption sites, promoting the electron transfer process for decomposition of the PS molecules to produce ROS. More interestingly, the peaks of S$_2$O$_8^{2-}$ vanished in the Co-N$_3$/WPAC+PS+SIZ system with the appearance of a new peak at 980 cm^{-1} for SO$_4^{2-}$, testifying that PS was consumed with the presence of SIZ. Thus, the Co-N$_3$/WPAC-PS* complex can effectively oxidize SIZ by direct electron transfer process, resulting in the O-O bond breaking and decomposition into SO$_4^{2-}$ [51]. The electron transfer between PS and Co-N$_3$/WPAC was further probed by electrochemical measurements. As shown in Fig. S13, the electrochemical impedance spectroscopy (EIS) Nyquist diagram of Co-N$_3$/-WPAC had a smaller arc radius as compared with the WPAC, indicating the smaller interfacial charge transfer resistance of Co-N$_3$/WPAC for catalysis. Fig. S14 monitored the current response of WPAC and Co-N$_3$/WPAC with the addition of PS. The instantaneous negative current response after adding PS suggested the rapid electron transfer from catalysts to PS. Furthermore, the evidently larger and more persistent current response of Co-N$_3$/WPAC to PS revealed more favorable electron transportation in the Co-N$_3$/WPAC+PS system, promoting efficient

generation of the ROS via PS activation.

In conclusion, the SIZ degradation in the Co-N$_3$/WPAC+PS system relied on the radical and non-radical pathways. On the one hand, PS could be effectively activated by the single atom Co sites to produce SO$_4^{•-}$ radical (Eqs. (1–3)) [52]. And the Co^{2+}/Co^{3+} cycles were maintained by the redox reaction of HSO$_5^-$ as described in Eqs. (3) and (4). Subsequently, the highly reactive SO$_4^{•-}$ in solution could react with H$_2$O to generate •OH through Eq. (5) [53]. Meanwhile, the [Co-N$_3$/WPAC-PS*] complex may be involved in the direct oxidation of pollutants by the extraction of electrons from SIZ molecules. Thus, both radical and non-radical mechanisms were involved in the Co-N$_3$/WPAC+PS system, leading to the efficient degradation of the various antibiotics in aqueous solution.

$$\equiv Co^{2+} + S_2O_8^{2-} \rightarrow \equiv Co^{3+} + SO_4^{•-} + SO_4^{2-} \tag{1}$$

$$S_2O_8^{2-} + H_2O \rightarrow HSO_5^- + HSO_4^- \tag{2}$$

$$\equiv Co^{2+} + HSO_5^- \rightarrow \equiv Co^{3+} + SO_4^{•-} + OH^- \tag{3}$$

$$\equiv Co^{3+} + HSO_5^- \rightarrow \equiv Co^{2+} + SO_5^{•-} + H^+ \tag{4}$$

$$SO_4^{•-} + H_2O \rightarrow HSO_4^- + •OH \, / \, SO_4^{2-} + •OH + H^+ \tag{5}$$
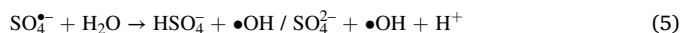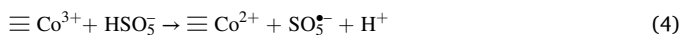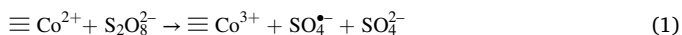
4. Conclusion

In summary, waste paper was creatively converted into carbon-supported SACs by loading of Co-N$_3$ single sites on the WPAC. The large specific surface area, porous structure, and single-atom Co dopants endowed the Co-N$_3$/WPAC catalyst with high adsorption capacity and

excellent catalytic performance for PS activation. The co-existence of radical ($\bullet$OH and $SO_4^{\bullet-}$) and non-radical (direct electron transfer) mechanisms was unveiled in the Co-N$_3$/WPAC+PS system. The coupled techniques promoted the preconcentration and in-situ oxidation of organic pollutants on the surface of Co-N$_3$/WPAC, leading to the efficient degradation and mineralization of SIZ in the Co-N$_3$/WPAC+PS system. In addition, the broad applicable pH range, low Co leaching and superior reusability and stability endowed the Co-N$_3$/WPAC catalyst with great application potential for practical wastewater treatment. This study provided a new and sustainable approach for waste paper recycling as well as the development of SACs for PS-AOPs.

CRediT authorship contribution statement

Mengying Qian: Data curation, Formal analysis, Writing & editing. **Meichi Lu:** Methodology, Data curation, Formal analysis. **Minjia Yan:** Methodology, Data curation, Formal analysis. **Chaofa Chen:** Methodology, Data curation. **Yuwen Hu:** Methodology, Data curation. **Yu Li:** Methodology, Data curation. **Jianrong Chen:** Methodology, Investigation, Funding acquisition. **Xi-Lin Wu:** Writing – review & editing, Supervision.

Declaration of Competing Interest

The authors declare that they have no known competing financial interests or personal relationships that could have appeared to influence the work reported in this paper.

Data Availability

Data will be made available on request.

Acknowledgments

Appendix A. Supporting information

Supplementary data associated with this article can be found in the online version at doi:10.1016/j.jece.2022.109219.

References

[1] G.G. Ying, L.Y. He, A.J. Ying, Q.Q. Zhang, Y.S. Liu, J.L. Zhao, China must reduce its antibiotic use, Environ. Sci. Technol. 51 (2017) 1072–1073.

[2] P. Kovalakova, L. Cizmas, T.J. McDonald, B. Marsalek, M. Feng, V.K. Sharma, Occurrence and toxicity of antibiotics in the aquatic environment: a review, Chemosphere 251 (2020), 126351.

[3] F. Chen, X.-L. Wu, L. Yang, C. Chen, H. Lin, J. Chen, Efficient degradation and mineralization of antibiotics via heterogeneous activation of peroxymonosulfate by using graphene supported single-atom Cu catalyst, Chem. Eng. J. 394 (2020), 124904.

[4] U. Hofer, The cost of antimicrobial resistance, Nat. Rev. Microbiol. 17 (2019) 3.

[5] L.-W. Yang, L.-H. She, Z.-H. Xie, Y.-L. He, X.-Y. Tian, C.-L. Zhao, Y.-Q. Guo, C. Hai, C.-S. He, B. Lai, Boosting activation of peracetic acid by Co@mZVI for efficient degradation of sulfamethoxazole: Interesting two-phase generation of reactive oxidized species, Chem. Eng. J. 448 (2022), 137667.

[6] Z. Wang, E. Almatrafi, H. Wang, H. Qin, W. Wang, L. Du, S. Chen, G. Zeng, P. Xu, Cobalt single atoms anchored on oxygen-doped tubular carbon nitride for efficient peroxymonosulfate activation: simultaneous coordination structure and morphology modulation, Angew. Chem. Int. Ed. 134 (2022), e202202338.

[7] Y. Lu, Y. Cai, S. Zhang, L. Zhuang, B. Hu, S. Wang, J. Chen, X. Wang, Application of biochar-based photocatalysts for adsorption-(photo)degradation/reduction of environmental contaminants: mechanism, challenges and perspective, Biochar 4 (2022) 45.

[8] C. Guo, C. Chen, J. Lu, D. Fu, C.Z. Yuan, X.L. Wu, K.N. Hui, J. Chen, Stable and recyclable Fe$_3$C@CN catalyst supported on carbon felt for efficient activation of peroxymonosulfate, J. Colloid Interf. Sci. 599 (2021) 219–226.

[9] J. Lu, C. Chen, M. Qian, P. Xiao, P. Ge, C. Shen, X.L. Wu, J. Chen, Hollow-structured amorphous prussian blue decorated on graphitic carbon nitride for

[10] Y. Liu, Z. Liu, Y. Wang, Y. Yin, J. Pan, J. Zhang, Q. Wang, Simultaneous absorption of SO$_2$ and NO from flue gas using ultrasound/Fe^{2+}/heat coactivated persulfate system, J. Hazard. Mater. 342 (2018) 326–334.

[11] N. Jiang, H. Xu, L. Wang, J. Jiang, T. Zhang, Nonradical oxidation of pollutants with single-atom-Fe(III)-activated persulfate: Fe(V) being the possible intermediate oxidant, Environ. Sci. Technol. 54 (2020) 14057–14065.

[12] L. Wang, J. Zhang, L. Zheng, J. Yang, Y. Li, X. Wan, X. Liu, X. Zhang, R. Yu, J. Shui, Carbon black-supported FM–N–C (FM = Fe, Co, and Ni) single-atom catalysts synthesized by the self-catalysis of oxygen-coordinated ferrous metal atoms, J. Mater. Chem. A 8 (2020) 13166–13172.

[13] H. Xu, H. Jia, H. Li, J. Liu, X. Gao, J. Zhang, M. Liu, D. Sun, S. Chou, F. Fang, R. Wu, Dual carbon-hosted Co-N$_3$ enabling unusual reaction pathway for efficient oxygen reduction reaction, Appl. Catal. B-Environ. 297 (2021), 120390.

[14] T. Yang, S. Fan, Y. Li, Q. Zhou, Fe-N/C single-atom catalysts with high density of Fe-Nx sites toward peroxymonosulfate activation for high-efficient oxidation of bisphenol A: electron-transfer mechanism, Chem. Eng. J. 419 (2021), 129590.

[15] X. Liu, G. Verma, Z. Chen, B. Hu, Q. Huang, H. Yang, S. Ma, X. Wang, Metal-organic framework nanocrystal-derived hollow porous materials: synthetic strategies and emerging applications, Innovation 3 (2022), 100281.

[16] X. Yue, T. Zhang, D. Yang, F. Qiu, Z. Li, Hybrid aerogels derived from banana peel and waste paper for efficient oil absorption and emulsion separation, J. Clean. Prod. 199 (2018) 411–419.

[17] X. Tang, G. Ran, J. Li, Z. Zhang, C. Xiang, Extremely efficient and rapidly adsorb methylene blue using porous adsorbent prepared from waste paper: kinetics and equilibrium studies, J. Hazard. Mater. 402 (2021), 123579.

[18] J. Yang, Z. Ao, H. Wu, S. Zhang, C. Chi, C. Hou, L. Qian, Waste paper-derived magnetic carbon composite: a novel eco-friendly solid acid for the synthesis of n-butyl levulinate from furfuryl alcohol, Renew, Energy 146 (2020) 477–483.

[19] X. Liang, D. Wang, Z. Zhao, T. Li, Z. Chen, Y. Gao, C. Hu, Engineering the low-coordinated single cobalt atom to boost persulfate activation for enhanced organic pollutant oxidation, Appl. Catal. B-Environ. 303 (2022), 120877.

[20] P. Xiao, P. Wang, H. Li, Q. Li, Y. Shi, X.L. Wu, H. Lin, J. Chen, X. Wang, New insights into bisphenols removal by nitrogen-rich nanocarbons: synergistic effect between adsorption and oxidative degradation, J. Hazard. Mater. 345 (2018) 123–130.

[21] Y. Li, L. Mu, Y.-S. Hu, H. Li, L. Chen, X. Huang, Pitch-derived amorphous carbon as high performance anode for sodium-ion batteries, Energy Storage Mater. 2 (2016) 139–145.

[22] H. Zhang, L. Lyu, Q. Fang, C. Hu, S. Zhan, T. Li, Cation−π structure inducing efficient peroxymonosulfate activation for pollutant degradation over atomically dispersed cobalt bonding graphene-like nanospheres, Appl. Catal. B-Environ. 286 (2021), 119912.

[23] W. Tian, H. Sun, X. Duan, H. Zhang, Y. Ren, S. Wang, Biomass-derived functional porous carbons for adsorption and catalytic degradation of binary micropollutants in water, J. Hazard. Mater. 389 (2020), 121881.

[24] X. Zhao, X. Li, Z. Zhu, W. Hu, H. Zhang, J. Xu, X. Hu, Y. Zhou, M. Xu, H. Zhang, G. Hu, Single-atom Co embedded in BCN matrix to achieve 100 % conversion of peroxymonosulfate into singlet oxygen, Appl. Catal. B-Environ. 300 (2022), 120759.

[25] H. Jing, Z. Zhao, J. Zhang, C. Zhu, W. Liu, N. Li, C. Hao, Y. Shi, D. Wang, Atomic evolution of metal–organic frameworks into Co–N$_3$ coupling vacancies by cooperative cascade protection strategy for promoting triiodide reduction, J. Phys. Chem. C 125 (2021) 6147–6156.

[26] J. Li, S. Zhao, L. Zhang, S.P. Jiang, S.Z. Yang, S. Wang, H. Sun, B. Johannessen, S. Liu, Cobalt single atoms embedded in nitrogen-doped graphene for selective oxidation of benzyl alcohol by activated peroxymonosulfate, Small 17 (2021), e2004579.

[27] K. Shah, R. Dai, M. Mateen, Z. Hassan, Z. Zhuang, C. Liu, M. Israr, W.C. Cheong, B. Hu, R. Tu, Cobalt single atom incorporated in ruthenium oxide sphere: a robust bifunctional electrocatalyst for HER and OER, Angew. Chem. 134 (2022), e202114951.

[28] C. Zhou, H. Zhou, Y. Yuan, J. Peng, G. Yao, P. Zhou, B. Lai, Coupling adsorption and in-situ Fenton-like oxidation by waste leather-derived materials in continuous flow mode towards sustainable removal of trace antibiotics, Chem. Eng. J. 420 (2021) 130370.

[29] J. Liu, H. He, Z. Shen, H.H. Wang, W. Li, Photoassisted highly efficient activation of persulfate over a single-atom Cu catalyst for tetracycline degradation: process and mechanism, J. Hazard. Mater. 429 (2022), 128398.

[30] Y. Li, Z. Yang, H. Zhang, X. Tong, J. Feng, Fabrication of sewage sludge-derived magnetic nanocomposites as heterogeneous catalyst for persulfate activation of Orange G degradation, Colloid Surf. A 529 (2017) 856–863.

[31] C. Xu, G. Yang, J. Li, S. Zhang, Y. Fang, F. Peng, S. Zhang, R. Qiu, Efficient purification of tetracycline wastewater by activated persulfate with heterogeneous Co-V bimetallic oxides, J. Colloid Interf. Sci. 619 (2022) 188–197.

[32] H. Zhang, L.C. Nengzi, Z. Wang, X. Zhang, B. Li, X. Cheng, Construction of Bi$_2$O$_3$/CuNiFe LDHs composite and its enhanced photocatalytic degradation of lomefloxacin with persulfate under simulated sunlight, J. Hazard. Mater. 383 (2020) 121236.

[33] Q. Ma, L.-c Nengzi, B. Li, Z. Wang, L. Liu, X. Cheng, Heterogeneously catalyzed persulfate with activated carbon coated with CoFe layered double hydroxide (AC@CoFe-LDH) for the degradation of lomefloxacin, Sep. Purif. Technol. 235 (2020), 116204.

photo-assisted activation of peroxymonosulfate, J. Colloid Interf. Sci. 603 (2021) 856–863.

[34] X. Li, Y. Jia, M. Zhou, X. Su, J. Sun, High-efficiency degradation of organic pollutants with Fe, N co-doped biochar catalysts via persulfate activation, J. Hazard. Mater. 397 (2020) 122764.

[35] J. Kang, X. Duan, L. Zhou, H. Sun, M.O. Tadé, S. Wang, Carbocatalytic activation of persulfate for removal of antibiotics in water solutions, Chem. Eng. J. 288 (2016) 399–405.

[36] L. Niu, G. Zhang, G. Xian, Z. Ren, T. Wei, Q. Li, Y. Zhang, Z. Zou, Tetracycline degradation by persulfate activated with magnetic γ-Fe$_2$O$_3$/CeO$_2$ catalyst: performance, activation mechanism and degradation pathway, Sep. Purif. Technol. 259 (2021), 118156.

[37] T. Zhang, Y. Liu, Y. Rao, X. Li, D. Yuan, S. Tang, Q. Zhao, Enhanced photocatalytic activity of TiO$_2$ with acetylene black and persulfate for degradation of tetracycline hydrochloride under visible light, Chem. Eng. J. 384 (2020), 123350.

[38] P. Huang, P. Zhang, C. Wang, J. Tang, H. Sun, Enhancement of persulfate activation by Fe-biochar composites: synergism of Fe and N-doped biochar, Appl. Catal. B-Environ. 303 (2022), 120926.

[39] D. Liu, M. Li, X. Li, F. Ren, P. Sun, L. Zhou, Core-shell Zn/Co MOFs derived Co$_3$O$_4$/CNTs as an efficient magnetic heterogeneous catalyst for persulfate activation and oxytetracycline degradation, Chem. Eng. J. 387 (2020), 124008.

[40] H. Li, Y. Liu, F. Jiang, X. Bai, H. Li, D. Lang, L. Wang, B. Pan, Persulfate adsorption and activation by carbon structure defects provided new insights into ofloxacin degradation by biochar, Sci. Total Environ. 806 (2022) 150968.

[41] J. Yao, Z. Chen, H. Zhang, N. Gao, Z. Zhang, W. Jiang, New insight into the regulation mechanism of visible light in naproxen degradation via activation of peroxymonosulfate by MOF derived BiFeO$_3$, J. Hazard. Mater. 431 (2022), 128513.

[42] W. Song, P. Ge, Q. Ke, Y. Sun, F. Chen, H. Wang, Y. Shi, X.L. Wu, H. Lin, J. Chen, C. Shen, Insight into the mechanisms for hexavalent chromium reduction and sulfisoxazole degradation catalyzed by graphitic carbon nitride: The Yin and Yang in the photo-assisted processes, Chemosphere 221 (2019) 166–174.

[43] H. Zhang, Z. Kang, J. Han, P. Wang, J. Fan, G. Sheng, Photothermal nanoconfinement reactor: boosting chemical reactivity with locally high temperature in confined space, Angew. Chem. 134 (2022), e202200093.

[44] Y. Gong, B. Yang, H. Zhang, X. Zhao, A g-C3N4/MIL-101(Fe) heterostructure composite for highly efficient BPA degradation with persulfate under visible light irradiation, J. Mater. Chem. A 6 (2018) 23703–23711.

[45] H. Lee, H.-J. Lee, J. Jeong, J. Lee, N.-B. Park, C. Lee, Activation of persulfates by carbon nanotubes: oxidation of organic compounds by nonradical mechanism, Chem. Eng. J. 266 (2015) 28–33.

[46] X. Duan, Z. Ao, H. Sun, L. Zhou, G. Wang, S. Wang, Insights into N-doping in single-walled carbon nanotubes for enhanced activation of superoxides: a mechanistic study, Chem. Commun. 51 (2015) 15249–15252.

[47] C. Guan, J. Jiang, C. Luo, S. Pang, C. Jiang, J. Ma, Y. Jin, J. Li, Transformation of iodide by carbon nanotube activated peroxydisulfate and formation of iodoorganic compounds in the presence of natural organic matter, Environ. Sci. Technol. 51 (2017) 479–487.

[48] C. Guan, J. Jiang, S. Pang, C. Luo, J. Ma, Y. Zhou, Y. Yang, Oxidation kinetics of bromophenols by nonradical activation of peroxydisulfate in the presence of carbon nanotube and formation of brominated polymeric products, Environ. Sci. Technol. 51 (2017) 10718–10728.

[49] T. Zhang, W. Li, J.P. Croue, Catalytic ozonation of oxalate with a cerium supported palladium oxide: an efficient degradation not relying on hydroxyl radical oxidation, Environ. Sci. Technol. 45 (2011) 9339–9346.

[50] T. Zhang, H. Zhu, J.P. Croue, Production of sulfate radical from peroxymonosulfate induced by a magnetically separable CuFe$_2$O$_4$ spinel in water: efficiency, stability, and mechanism, Environ. Sci. Technol. 47 (2013) 2784–2791.

[51] W. Ren, L. Xiong, X. Yuan, Z. Yu, H. Zhang, X. Duan, S. Wang, Activation of peroxydisulfate on carbon nanotubes: Electron-transfer mechanism, Environ. Sci. Technol. 53 (2019) 14595–14603.

[52] X. Pan, L. Yan, C. Li, R. Qu, Z. Wang, Degradation of UV-filter benzophenone-3 in aqueous solution using persulfate catalyzed by cobalt ferrite, Chem. Eng. J. 326 (2017) 1197–1209.

[53] M. Izadifard, G. Achari, C.H. Langford, Degradation of sulfolane using activated persulfate with UV and UV-Ozone, Water Res. 125 (2017) 325–331.